Treatment of Dirichlet-type boundary conditions in the spline-based wavelet Galerkin method employing multiple point constraints

Shogo Sannomaru[a], Satoyuki Tanaka[a],
Ken-ichiro Yoshida[a], Tinh Quoc Bui[b],
Shigenobu Okazawa[c], Seiya Hagihara[d]

[a] *Graduate School of Engineering, Hiroshima University, Japan,*
e-mail: d126490@hiroshima-u.ac.jp, satoyuki@hiroshima-u.ac.jp,
m143894@hiroshima-u.ac.jp
[b] *Department of Civil and Environmental Engineering,*
Tokyo Institute of Technology, Japan, e-mail: tinh.buiquoc@gmail.com
[c] *Division of Mechanical Engineering, Faculty of Engineering,*
University of Yamanashi, Japan, e-mail: sokazawa@yamanashi.ac.jp
[d] *Department of Mechanical Engineering, Saga University,*
Japan, e-mail: hagihara@me.saga-u.ac.jp

Abstract

The wavelet methods have been extensively adopted and integrated in various numerical methods to solve partial differential equations. The wavelet functions, however, do not satisfy the Kronecker delta function properties, special treatment methods for imposing the Dirichlet-type boundary conditions are thus required. It motivates us to present in this paper a novel treatment technique for the essential boundary conditions (BCs) in the spline-based wavelet Galerkin method (WGM), taking the advantages of the multiple point constraints (MPCs) and adaptivity. The linear B-spline scaling function and multilevel wavelet functions are employed as basis functions. The effectiveness of the present method is addressed, and in particular the applicability of the MPCs is also investigated. In the proposed technique, MPC equations based on the tying relations of the wavelet basis functions along the essential BCs are developed. The stiffness matrix is degenerated based on the MPC equations to impose the BCs. The numerical implementation is simple, and no additional degrees of freedom are needed in the system of linear equations. The accuracy of the present formulation in treating the BCs in the WGM is high, which is illustrated through a number of representative numerical examples including an adaptive analysis.

Keywords: Wavelet Galerkin Method; Meshfree Method; Multiple Point Constraints; Adaptive Analysis.

---

1. Introduction

Wavelet methods [1-4] have been widely adopted for signal/image denoising and data compression. One of their unique advantages is the availability of multiresolution analysis (MRA), which allows easy control of spatial and time resolution. In recent years, wavelet methods have also been applied to solving partial differential equations, for which the spatial resolution of the analysis model can easily be controlled due to MRA. So far, the wavelet collocation method [5-9], wavelet boundary element method [10-12], wavelet finite element method (FEM) [13-20] and wavelet Galerkin method (WGM) [21-24] are some that have proposed to solve engineering problems. Li and Chen have categorized and classified the wavelet-based numerical methods in [25]. The present study focuses on the WGM.

When solving boundary value problems using WGMs, the problem domain is discretized, quite often, by equally spaced grids or structured cells, and refinements of the solution are obtained by applying the MRA to the wavelet basis functions. Because wavelet Galerkin (WG) modeling reduces its model generation tasks, the methods can be categorized as meshfree methods. Several boundary value problems have been successfully addressed using WGMs, including the layout optimization problem [26], elastic-plastic-damage analysis [27], the plate bending problem [28] and analysis of electric field distribution [29]. Our previous work developed an adaptive strategy for problems in solid mechanics [30], and two-dimensional (2D) fracture mechanics problems were analyzed in [31-34] using B-spline scaling/wavelet functions.

Despite advances in the development of the WG approaches, difficulties remain in treating the essential boundary conditions (BCs). Several techniques have been proposed, *e.g.*, imposing periodic BCs [21], the use of boundary-corrected wavelet bases [27], the fictitious domain approach [35], and wavelet-based FEM [36-37]. Meshfree methods sometimes handle BCs less than optimally, because most meshfree interpolants do not possess the so-called Kronecker delta property. A special treatment is then needed to enforce the essential BCs. So far, the Lagrange multiplier method [38], penalty method [39-41], modified variational principle [42], multiple point constraints (MPCs) [43-45] and modification of meshfree interpolation functions [46] have been employed. Additionally, a meshfree interpolant possessing the Kronecker delta property has been proposed in [47-49]. Because the B-spline wavelet bases generally do not, aside from the linear B-spline scaling function, have Kronecker delta property, a penalty formulation was employed in [30-32]. The formulation is simple and easy to implement in the computer program as compared to other techniques. However, the stiffness matrix becomes ill-conditioned. An alternative technique is needed to impose the essential BCs for analyzing practical engineering applications using the WGM.

In the present study, the MPCs are applied to the spline-based WGM. The tying equations of the wavelet basis functions are derived based on the essential BCs. The stiffness matrix is degenerated with the MPC equations to impose the BCs. The method is simple but effective. The condition number of the stiffness matrix will be improved compare with the penalty formulation, and no additional degrees of freedom (DOFs) are needed in the system of linear simultaneous equations. Although it has been reported [45] that accuracy deteriorates near the boundaries when applying MPCs in meshfree methods, the spline-based wavelet basis functions here have simple functional forms and are located equidistantly in the analysis domain. Furthermore, they have so called two-scale relations, *i.e.*, the scaling/wavelet functions can be represented using scaling functions at a resolution that is one-step higher. Here the functional shapes and arrangements of the scaling and multilevel wavelet functions are critically examined, and it is found that a simple tying equation for the wavelet basis functions can be derived when imposing the essential BCs by means of MPCs. The applicability of this approach to 2D solid mechanics problems is investigated, and the accuracy with which the BCs are enforced is discussed through the several numerical examples.

This paper is arranged as follows: Spline-based WGM is briefly presented in Section 2. In Section 3, MPCs are introduced in the WGM, and their applicability is validated with a simple 2D problem. Several numerical examples, including an adaptive analysis, are presented in Section 4 and Section

5, concluding remarks are addressed.

2. Spline-based WGM

2.1. Linear B-spline scaling/wavelet functions

A boundary value problem for 2D elastostatic analysis and the discretization with the spline-based WGM are presented. Because function shapes of the linear B-spline wavelet bases are needed to discuss the enforcement of the essential BCs employing the MPCs, mathematical representations of the function forms and the two-scale relations are reviewed first.

One-dimensional (1D) linear B-spline scaling function $\phi(x)$ and wavelet function $\psi(x)$ are schematically depicted in Fig.1(a). They have so-called two-scale relation in wavelet theory, *i.e.*, the scaling/wavelet functions are represented by superposition of the one-step higher resolution scaling functions. The schematic illustrations for the scaling/wavelet functions are presented in Fig.1(b). They have following two-scale relations with the coefficients, as:

$$\begin{aligned} \phi(x) =& \frac{1}{2}\phi(2x) + \phi(2x-1) + \frac{1}{2}\phi(2x-2), \qquad (1) \\ \psi(x) =& \frac{1}{12}\phi(2x) - \frac{1}{2}\phi(2x-1) + \frac{5}{6}\phi(2x-2) \\ & - \frac{1}{2}\phi(2x-3) + \frac{1}{12}\phi(2x-4). \qquad (2) \end{aligned}$$

Otherwise, the scaling function can be rewritten by a polynomial form, as:

$$\phi(x) = \left\{ \begin{array}{cc} x, & 0 \leq x < 1 \\ 2-x, & 1 \leq x \leq 2 \end{array} \right. , \qquad (3)$$

and for the wavelet function, as:

$$\psi(x) = \left\{ \begin{array}{cc} \frac{1}{6}x, & 0 \leq x < 0.5 \\ -\frac{7}{6}x + \frac{2}{3}, & 0.5 \leq x < 1 \\ \frac{8}{3}x - \frac{19}{6}, & 1 \leq x < 1.5 \\ -\frac{8}{3}x + \frac{29}{6}, & 1.5 \leq x < 2 \\ \frac{7}{6}x - \frac{17}{6}, & 2 \leq x < 2.5 \\ -\frac{1}{6}x + \frac{1}{2}, & 2.5 \leq x \leq 3 \end{array} \right. . \qquad (4)$$

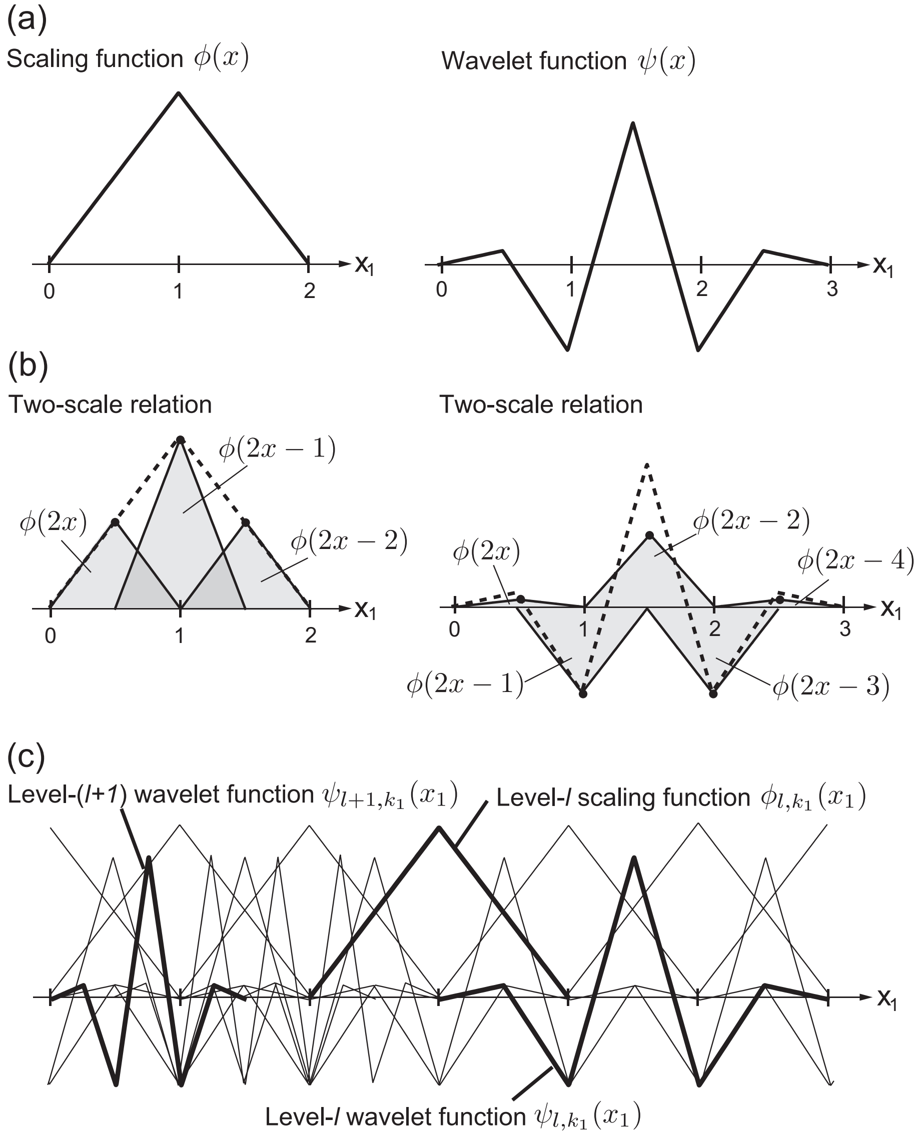

Figure 1: 1D linear scaling/wavelet functions: (a) Function shapes, (b) Two-scale relations and (c) Arrangements of the multilevel wavelet bases in the WGM (Lelvel-$(l+2)$ model).

In the WGM, the scaling/wavelet functions are adopted as the basis functions. Here, the lowest resolution is assumed as the resolution level-l, and a function space composed of the level-l scaling functions $\phi^{l}_{k_1}(x_1)$ (l, $k_1 \in \mathbb{Z}$) is called the level-l model. k_1 is a 1D translation parameter. To improve the accuracy of the solution, the level-l, -$(l+1)$, $\cdots$ wavelet functions $\psi^{l}_{k_1}(x_1)$, $\psi^{l+1}_{k_1}(x_1)$, $\cdots$ are added to the level-l model, and these are called the level-$(l+1)$, -$(l+2)$, $\cdots$ models, respectively.

A schematic of the 1D level-$(l+2)$ model is shown in Fig.1(c). A 1D function $f(x_1)$ can thus be written employing the level-$(l+2)$ model as,

$$f^{l+2}(x_1) = \sum_{k_1 \in \mathbb{Z}} a^{l}_{k_1} \phi^{l}_{k_1}(x_1) + \sum_{k_1 \in \mathbb{Z}} b^{l}_{k_1} \psi^{l}_{k_1}(x_1) + \sum_{k_1 \in \mathbb{Z}} b^{l+1}_{k_1} \psi^{l+1}_{k_1}(x_1), \tag{5}$$

where $f^{l+2}(x_1)$ is an approximated value of $f(x_1)$ at level-$(l+2)$. As the level of the wavelet functions shift from level-l to -$(l+1)$, the function support becomes half. Because the spatial resolution can be controlled by adding higher-resolution wavelet functions, adaptive refinements are easy to perform without remeshing. Noted that when employing the level-l scaling/wavelet functions and the level-$(l+1)$ wavelet functions on the entire domain in Eq.(5), the results are equivalent to those of the level-$(l+2)$ scaling functions, *i.e.*,

$$f^{l+2}(x_1) = \sum_{k_1 \in \mathbb{Z}} a^{l+2}_{k_1} \phi^{l+2}_{k_1}(x_1). \tag{6}$$

This is the so-called MRA in the wavelet theory. Further information of the linear B-spline scaling/wavelet functions including intervals and positions of the basis functions in the 1D and 2D WGM is detailed in [30-31].

2.2. WGM

A boundary value problem for elastostatics is analyzed using the WGM. A schematic illustration of the WG discretization is presented in Fig.2. The analysis domain is Ω and its boundary Γ. The domain is divided into equally spaced grids or structured cells. The essential BCs $\boldsymbol{u}=\bar{\boldsymbol{u}}$ is enforced on Γ_u, and the traction BCs $\boldsymbol{t}=\bar{\boldsymbol{t}}$ is set on Γ_t, such that $\Gamma=\Gamma_u \cup \Gamma_t$ and $\Gamma_u \cap \Gamma_t = \emptyset$. The external boundaries are represented with a sub-cell approach. A structured cell (level-l cell) is divided into $ndiv \times ndiv$ sub-cells, numerical integration of the stiffness matrix is performed when the central coordinate of a sub-cell is located in the analysis domain. To improve the accuracy of the solution such as around a hole, the multilevel wavelet functions are superposed locally on the low-resolution model.

The governing equation for the elastostatic body is

$$\boldsymbol{L}^T \boldsymbol{D} \boldsymbol{L} \boldsymbol{u} - \boldsymbol{f} = \boldsymbol{L}^T \boldsymbol{\sigma} - \boldsymbol{f} = 0 \quad in \quad \Omega, \tag{7}$$

where $\boldsymbol{D}$ is the elasticity matrix and $\boldsymbol{L}$ is a differential operator that defines the strain as:

$$\boldsymbol{\epsilon} = \boldsymbol{L}\boldsymbol{u}. \tag{8}$$

The stresses are evaluated from the displacement vector $\boldsymbol{u}$ by differentiation

$$\boldsymbol{\sigma} = \boldsymbol{D}\boldsymbol{L}\boldsymbol{u}. \tag{9}$$

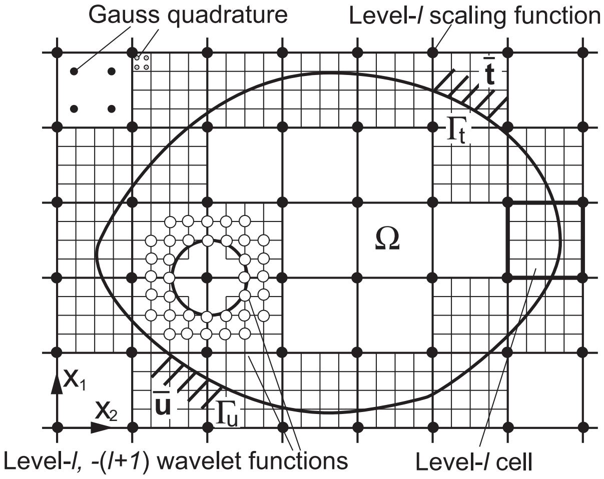

Figure 2: Boundary value problem for elastostatics and the WG discretization.

In the WGM, the displacement $\boldsymbol{u}(\boldsymbol{x})$ is approximated by the scaling functions and the multilevel wavelet functions. For examples, the level-$(l+2)$ displacement $\boldsymbol{u}^{l+2}(\boldsymbol{x})$ $(=\{u_1^{l+2}(\boldsymbol{x}), u_2^{l+2}(\boldsymbol{x})\}^T)$ is expressed as:

$$\begin{aligned} \boldsymbol{u}^{l+2}(\boldsymbol{x}) = & \sum_{k_1,k_2 \in \mathbb{Z}} \boldsymbol{a}^l_{k_1,k_2} \boldsymbol{\Phi}^l_{k_1,k_2}(\boldsymbol{x}) + \sum_{i=1}^{3} \sum_{k_1,k_2 \in \mathbb{Z}} \boldsymbol{b}^{l,i}_{k_1,k_2} \boldsymbol{\Psi}^{l,i}_{k_1,k_2}(\boldsymbol{x}) \\ & + \sum_{i=4}^{8} \sum_{k_1,k_2 \in \mathbb{Z}} \boldsymbol{b}^{l+1,i}_{k_1,k_2} \boldsymbol{\Psi}^{l+1,i}_{k_1,k_2}(\boldsymbol{x}), \end{aligned} \tag{10}$$

where $\boldsymbol{\Phi}^{l}_{k_1,k_2}(\boldsymbol{x})$ is the 2D level-l scaling functions, $\boldsymbol{\Psi}^{l,i}_{k_1,k_2}(\boldsymbol{x})$ and $\boldsymbol{\Psi}^{l+1,i}_{k_1,k_2}(\boldsymbol{x})$ are the level-l and -$(l+1)$ wavelet functions, respectively. i $(\in \mathbb{Z})$ is a number of the 2D wavelet functions. k_1 and k_2 $(\in \mathbb{Z})$ are 2D translation parameters which depends on the position of the 2D scaling/wavelet functions. $\boldsymbol{a}^{l}_{k_1,k_2}$ $(=\{a^{l}_{1,k_1,k_2}, a^{l}_{2,k_1,k_2}\}^T)$, $\boldsymbol{b}^{l,i}_{k_1,k_2}$ $(=\{b^{l,i}_{1,k_1,k_2}, b^{l,i}_{2,k_1,k_2}\}^T)$ and $\boldsymbol{b}^{l+1,i}_{k_1,k_2}$ $(=\{b^{l+1,i}_{1,k_1,k_2}, b^{l+1,i}_{2,k_1,k_2}\}^T)$ are their coefficient vectors. When employing the level-l and -$(l+1)$ wavelet functions on the entire domain, the level-$(l+2)$ displacement $\boldsymbol{u}^{l+2}(\boldsymbol{x})$ with Eq.(10) is equivalent to that of the level-$(l+2)$ scaling functions only, *i.e.*,

$$\boldsymbol{u}^{l+2}(\boldsymbol{x}) = \sum_{k_1,k_2\in\mathbb{Z}} \boldsymbol{a}^{l+2}_{k_1,k_2}\boldsymbol{\Phi}^{l+2}_{k_1,k_2}(\boldsymbol{x}), \tag{11}$$

where $\boldsymbol{\Phi}^{l+2}_{k_1,k_2}(\boldsymbol{x})$ and $\boldsymbol{a}^{l+2}_{k_1,k_2}$ are the level-$(l+2)$ scaling functions and the coefficients, respectively. The 2D basis functions are obtained by multiplying the 1D scaling/wavelet functions [30]. The results and DOFs of both the analyses in Eqs.(10) and (11) are exactly same when the basis functions are adopted on entire the analysis domain.

In the wavelet method, the wavelet functions assume continuous on the entire domain. Therefore, domain bounded functions are sometime generated when analyzing the boundary value problems. In the spline-based WGM, lack of linear independency occurs in the linear simultaneous equation due to the domain bounded functions. The author's previous study, a technique to remove the domain bounded scaling/wavelet functions that can be represented by the superposition of the other basis functions were proposed in [30].

Substituting Eq.(10) into Eq.(7), following linear simultaneous equation is obtained:

$$\boldsymbol{K}_{l+2}\boldsymbol{U}_{l+2} = \boldsymbol{f}_{l+2}, \tag{12}$$

where $\boldsymbol{K}_{l+2}$ is the stiffness matrix, $\boldsymbol{U}_{l+2}$ is the displacement vector and $\boldsymbol{f}_{l+2}$ is the traction vector at level-$(l+2)$. The entries of the stiffness matrix and traction vector are

$$\boldsymbol{K}_{l+2} = \int_{\Omega} \boldsymbol{B}^T_{l+2}\boldsymbol{D}\boldsymbol{B}_{l+2}\, d\Omega, \tag{13}$$

$$\boldsymbol{f}_{l+2} = \int_{\Gamma_u} \boldsymbol{N}^T_{l+2}\bar{\boldsymbol{t}}\, d\Gamma_t, \tag{14}$$

where $\boldsymbol{B}_{l+2}$ is a displacement gradient matrix and $\boldsymbol{N}_{l+2}$ is a matrix of shape functions at level-$(l+2)$. The stiffness matrix and traction vector are numerically integrated using Gauss quadrature based on the cells and sub-cells as illustrated in Fig.2. Further details of the WG discretization can be found in [30-31]. When adopting MPCs to impose the essential BCs, the stiffness matrix is degenerated based on the MPC equations along the essential BCs, and no additional terms are needed. The detail is described in Section 3.

For the comparison purposes, a penalty formulation is also employed to impose the essential BCs. The linear simultaneous equation is written as:

$$(\boldsymbol{K}_{l+2} + \boldsymbol{K}^{\alpha}_{l+2})\boldsymbol{U}_{l+2} = \boldsymbol{f}_{l+2} + \boldsymbol{f}^{\alpha}_{l+2}, \tag{15}$$

where $\boldsymbol{K}^{\alpha}_{l+2}$ and $\boldsymbol{f}^{\alpha}_{l+2}$ are a matrix and a vector pertaining to the penalty term. They are represented, as:

$$\boldsymbol{K}^{\alpha}_{l+2} = \alpha \int_{\Gamma_u} \boldsymbol{N}^{T}_{l+2}\boldsymbol{N}_{l+2}\, d\Gamma_u, \tag{16}$$

$$\boldsymbol{f}^{\alpha}_{l+2} = \alpha \int_{\Gamma_u} \boldsymbol{N}^{T}_{l+2}\bar{\boldsymbol{u}}\, d\Gamma_u, \tag{17}$$

with the coefficient α a large positive number.

3. Treatment of essential BCs using the MPCs

3.1. A test problem

The applicability of the MPCs in the WGM is demonstrated through a simple 2D problem of a 2.0×2.0 (mm) square plate, which is subjected to a uniform pressure at the top edge as depicted in Fig.3. The material parameters of plate are: The Young's modulus E=1.0 (MPa) and the Poisson's ratio ν=0.3. The problem being studied is assumed to be plane stress condition. As the essential BCs, displacements of x_2-direction $u_2(\boldsymbol{x})$ is fixed along the bottom of the plate (x_2=0.0), and displacements of x_1-direction $u_1(\boldsymbol{x})$ is fixed along the left side of the plate (x_1=0.0). Therefore, a uniform strain field will be obtained.

To discuss enforcement of the essential BCs using the MPCs, the wavelet interpolants along the BCs are critically investigated. The level-l scaling and wavelet functions are adopted as the basis functions, *i.e.*, this is the level-$(l+1)$ model. The 2D wavelet basis functions are obtained by multiplying the 1D scaling/wavelet functions as:

$$
\begin{aligned}
\boldsymbol{\Phi}^{l}_{k_1,k_2}(x_1,x_2) &= \phi^{l}_{k_1}(x_1)\phi^{l}_{k_2}(x_2),\\
\boldsymbol{\Psi}^{l,1}_{k_1,k_2}(x_1,x_2) &= \psi^{l}_{k_1}(x_1)\phi^{l}_{k_2}(x_2),\\
\boldsymbol{\Psi}^{l,2}_{k_1,k_2}(x_1,x_2) &= \phi^{l}_{k_1}(x_1)\psi^{l}_{k_2}(x_2),\\
\boldsymbol{\Psi}^{l,3}_{k_1,k_2}(x_1,x_2) &= \psi^{l}_{k_1}(x_1)\psi^{l}_{k_2}(x_2).
\end{aligned}
\tag{18}
$$

For the simple representation, superscript "l" in the wavelet bases and the coefficients of Eq.(10) are abbreviated. And, subscripts "k_1, k_2" substitute the node number "k" of the 2D basis functions, *i.e.*, $\boldsymbol{a}^{l}_{k_1,k_2}$, $\boldsymbol{b}^{l,i}_{k_1,k_2}$, $\boldsymbol{\Phi}^{l}_{k_1,k_2}$ and $\boldsymbol{\Psi}^{l,i}_{k_1,k_2}$ become $\boldsymbol{a}_k(=\{a_{1,k}, a_{2,k}\}^T)$, $\boldsymbol{b}^{i}_{k}(=\{b^{i}_{1,k}, b^{i}_{2,k}\}^T)$, $\boldsymbol{\Phi}_k$ and $\boldsymbol{\Psi}^{i}_{k}$, respectively.

The central coordinates of the wavelet bases (nodes) are presented in Fig.3. The scaling functions $\boldsymbol{\Phi}_k$ (k=1, $\cdots$, 4) are located on the corners of the plate. The wavelet functions $\boldsymbol{\Psi}^{1}_{k}$ (k=5, 6) and $\boldsymbol{\Psi}^{2}_{k}$ (k=7, 8) are located on the edges of the plate. The wavelet function $\boldsymbol{\Psi}^{3}_{k}$ (k=9) is set to be located at the center of the plate, as shown in Fig.3. Although the wavelet functions which are located external the rectangular region span the analysis domain, the stiffness matrix becomes singular when it includes them. They should be excluded employing a technique proposed in [30].

Enforcing the essential BCs along the bottom of the plate requires that zero displacement ($u_2(\boldsymbol{x})$=0.0) holds for $0.0 \le x_1 < 2.0$, with a linear combination of wavelet basis functions. The function shapes along x_2=0.0 are presented in Fig.4. The scaling functions $\boldsymbol{\Phi}_1$, $\boldsymbol{\Phi}_2$ and wavelet functions $\boldsymbol{\Psi}^{1}_{5}$, $\boldsymbol{\Psi}^{2}_{7}$, $\boldsymbol{\Psi}^{2}_{8}$ and $\boldsymbol{\Psi}^{3}_{9}$ are non-zero, but zero displacement can be achieved by superposing the scaling/wavelet functions on the bottom of the plate. The equation is written as

$$
\begin{aligned}
u_2(x_1,0) = {} & a_{2,1}\boldsymbol{\Phi}_1 + a_{2,2}\boldsymbol{\Phi}_2\\
& + b^{1}_{2,5}\boldsymbol{\Psi}^{1}_{2,5} + b^{2}_{2,7}\boldsymbol{\Psi}^{2}_{2,7} + b^{2}_{2,8}\boldsymbol{\Psi}^{2}_{2,8} + b^{3}_{2,9}\boldsymbol{\Psi}^{3}_{2,9} = 0.0,\\
& 0.0 \le x_1 < 2.0.
\end{aligned}
\tag{19}
$$

where $a_{2,1}, a_{2,2}, b^{1}_{2,5}, b^{2}_{2,7}, b^{2}_{2,8}$ and $b^{3}_{2,9}$ are coefficients of the basis functions.

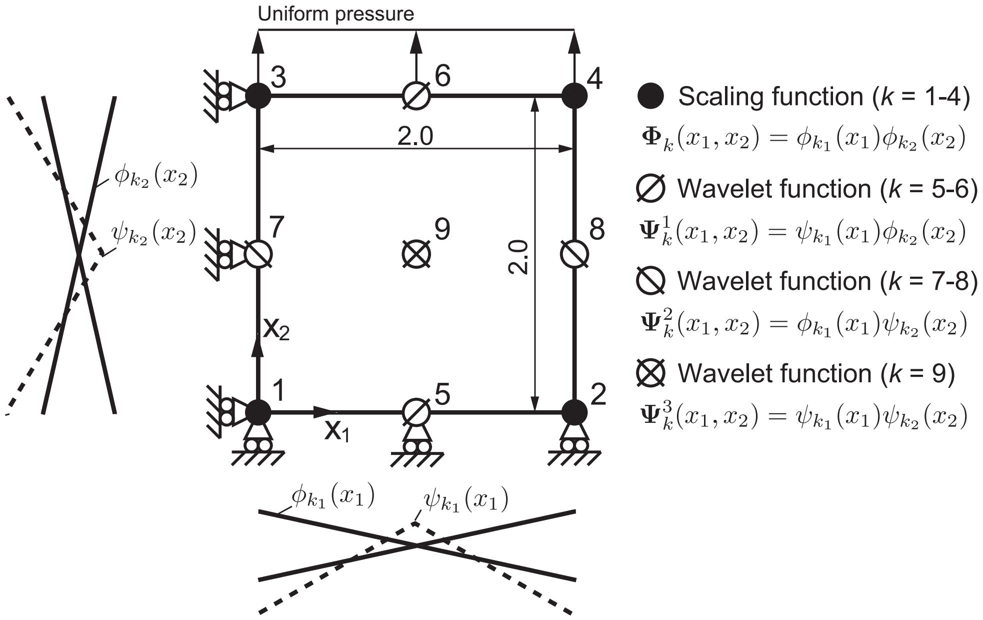

Figure 3: 2D test problem (Level-(l+1) model).

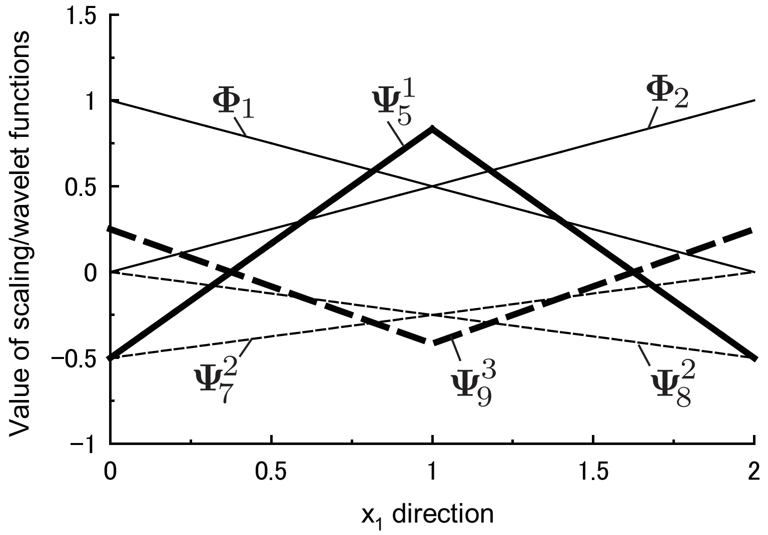

Figure 4: Scaling and wavelet basis functions along the bottom of the plate (x_2=0.0).

First, we focus on the two wavelet functions $\mathbf{\Psi}_5^1$ and $\mathbf{\Psi}_9^3$ in Eq.(19). They should cancel each other in imposing the essential BC, because they have a kink at x_1=1.0. The function shapes are represented as:

$$\mathbf{\Psi}_5^1(x_1,0)=\left\{\begin{array}{ll} \frac{4}{3}x_1-\frac{1}{2}, & 0\le x_1<1.0 \\ -\frac{4}{3}x_1+\frac{13}{6}, & 1.0\le x_1<2.0 \end{array}\right., \tag{20}$$

$$\mathbf{\Psi}_9^3(x_1,0)=\left\{\begin{array}{ll} -\frac{2}{3}x_1+\frac{1}{4}, & 0\le x_1<1.0 \\ \frac{2}{3}x_1-\frac{13}{12}, & 1.0\le x_1<2.0 \end{array}\right.. \tag{21}$$

From the relation of Eqs.(20) and (21), the basis functions will be vanished when their coefficients have a relation as

$$b_{2,5}^1 : b_{2,9}^3 = 2 : 1. \tag{22}$$

The other basis functions $\mathbf{\Phi}_1$, $\mathbf{\Phi}_2$, $\mathbf{\Psi}_7^2$ and $\mathbf{\Psi}_8^2$ in Eq.(19) are then examined. They monotonically increase/decrease in the area 0.0≤x_1<2.0. The function shapes are respectively written, as:

$$\begin{aligned}&\mathbf{\Phi}_1(x_1,0)=-\frac{1}{2}x_1+1, \quad \mathbf{\Phi}_2(x_1,0)=\frac{1}{2}x_1,\\ &\mathbf{\Psi}_7^2(x_1,0)=\frac{1}{4}x_1-\frac{1}{2}, \quad \mathbf{\Psi}_8^2(x_1,0)=-\frac{1}{4}x_1, \quad 0.0\le x_1<2.0.\end{aligned} \tag{23}$$

Employing Eqs.(22) and (23), and substituting into Eq.(19) and after rearranging the equation, following identical equation is obtained

$$u_2(x_1,0)=\left(-\frac{1}{2}a_{2,1}+\frac{1}{2}a_{2,2}+\frac{1}{4}b_{2,7}^2-\frac{1}{4}b_{2,8}^2\right)x_1+\left(a_{3,1}-\frac{1}{2}b_{2,7}^2\right)=0.0. \tag{24}$$

If Eq.(24) is always practical, the following relations can be derived:

$$a_{2,1} : b_{2,7}^2 = 2 : 1 \quad \text{and} \quad a_{2,2} : b_{2,8}^2 = 2 : 1. \tag{25}$$

The coefficients $a_{2,1} : b_{2,7}^2$, $a_{2,2} : b_{2,8}^2$ and $b_{2,5}^1 : b_{2,9}^3$ have the ratio of 2:1 on the boundary x_2=0.0.

3.2. Numerical implementation

Based on the above discussion, the MPC equations developed in the WGM are derived for every nodes of the scaling/wavelet functions located on the essential BCs. When imposing the essential BC $u_2(\boldsymbol{x})$=0 along the bottom line in Fig.3, the following equations are made on the nodes m=1, 2 and 5, *i.e.*,

$$u_2(\boldsymbol{x}_m) = \sum_k a_{2,k} \boldsymbol{\Phi}_k(\boldsymbol{x}_m) + \sum_{i=1}^{3} \sum_k b_{2,k}^i \boldsymbol{\Psi}_k^i(\boldsymbol{x}_m), \quad (m = 1, 2, 5), \tag{26}$$

where $\boldsymbol{x}_m$ is the position vector of node m. The displacement $u_2(\boldsymbol{x}_m)$ in Eq.(26) can be represented in matrix form as

$$\boldsymbol{u}_2 = \boldsymbol{N}\boldsymbol{v}_2 = \boldsymbol{c}, \tag{27}$$

where $\boldsymbol{u}_2$ is the displacement vector on the essential BCs. $\boldsymbol{N}$ and $\boldsymbol{v}_2$ are the matrix of the wavelet bases and the coefficient vector in terms of the enforcement, and $\boldsymbol{c}$ is a vector of an enforced value. The vectors $\boldsymbol{u}_2$ and $\boldsymbol{v}_2$ are given by:

$$\boldsymbol{u}_2 = \{u_2(\boldsymbol{x}_1), u_2(\boldsymbol{x}_2), u_2(\boldsymbol{x}_5)\}^T, \tag{28}$$
$$\boldsymbol{v}_2 = \{a_{2,1}, a_{2,2}, b_{2,5}^1, b_{2,7}^2, b_{2,8}^2, b_{2,9}^3\}^T. \tag{29}$$

and the matrix $\boldsymbol{N}$ is

$$\boldsymbol{N} = \{\boldsymbol{N}(\boldsymbol{x}_1), \boldsymbol{N}(\boldsymbol{x}_2), \boldsymbol{N}(\boldsymbol{x}_5)\}^T, \tag{30}$$
$$\boldsymbol{N}(\boldsymbol{x}_m) = \{\boldsymbol{\Phi}_1(\boldsymbol{x}_m), \boldsymbol{\Phi}_2(\boldsymbol{x}_m), \boldsymbol{\Psi}_5^1(\boldsymbol{x}_m), \boldsymbol{\Psi}_7^2(\boldsymbol{x}_m), \boldsymbol{\Psi}_8^2(\boldsymbol{x}_m), \boldsymbol{\Psi}_9^3(\boldsymbol{x}_m)\}. \tag{31}$$

The functions $\boldsymbol{\Phi}_1(\boldsymbol{x}_m)$, $\boldsymbol{\Phi}_1(\boldsymbol{x}_m)$ and $\boldsymbol{\Psi}_5^1(\boldsymbol{x}_m)$ are excluded in the matrix $\boldsymbol{N}$ and vector $\boldsymbol{v}_2$ because the functions are zero for x_2=0. A fundamental operation with pivot is carried out for Eq.(27). After rearrangement, the following relation is obtained,

$$\tilde{\boldsymbol{u}}_2 = -\boldsymbol{T}\tilde{\boldsymbol{v}}_2 + \tilde{\boldsymbol{c}}. \tag{32}$$

where $\tilde{\boldsymbol{u}}_2$, $\tilde{\boldsymbol{v}}_2$ and $\tilde{\boldsymbol{c}}$ correspond to the vectors in Eq.(27). $\boldsymbol{T}$ is a matrix after the fundamental operation of $\boldsymbol{N}$. From Eq.(32), the dependent vector $\tilde{\boldsymbol{u}}_2$ is represented by the tensor product $\boldsymbol{T}\tilde{\boldsymbol{v}}_2$ and the vector $\tilde{\boldsymbol{c}}$. This is a MPC equation in the WGM. The MPC equations along the left side of the plate are derived similarly.

Based on the MPC equations, the stiffness matrix and the force vector are degenerated. The linear simultaneous equation at level-$(l + 1)$ can be written, as:

$$\boldsymbol{K}_{l+1}\boldsymbol{U}_{l+1} = \boldsymbol{f}_{l+1}. \tag{33}$$

The displacement vector $\boldsymbol{U}_{l+1}$ is decomposed into dependent DOFs $\boldsymbol{U}_D$, independent DOFs $\boldsymbol{U}_I$ and unrelated DOFs $\boldsymbol{U}_O$. Employing the MPC equations, the vector $\boldsymbol{U}_{l+1}$ is represented as the tensor product of the transformation matrix $\boldsymbol{C}$ and the coefficient vector $\boldsymbol{V}_{l+1}$:

$$\boldsymbol{U}_{l+1} = \begin{Bmatrix} \boldsymbol{U}_D \\ \boldsymbol{U}_I \\ \boldsymbol{U}_O \end{Bmatrix} = \begin{bmatrix} \boldsymbol{I} & -\boldsymbol{T} & 0 \\ 0 & \boldsymbol{I} & 0 \\ 0 & 0 & \boldsymbol{I} \end{bmatrix} \begin{Bmatrix} \tilde{\boldsymbol{c}} \\ \boldsymbol{V}_I \\ \boldsymbol{V}_O \end{Bmatrix} = \boldsymbol{C}\boldsymbol{V}_{l+1}, \tag{34}$$

where $\boldsymbol{V}_I$ and $\boldsymbol{V}_O$ are vectors in terms of the independent DOFs and the unrelated DOFs. Adopting the relation of Eq.(34) to the virtual work principle, we obtain

$$\boldsymbol{K}'_{l+1}\boldsymbol{V}_{l+1} = \boldsymbol{f}'_{l+1}, \tag{35}$$

where $\boldsymbol{K}'_{l+1}(=\boldsymbol{C}^T\boldsymbol{K}_{l+1}\boldsymbol{C})$ and $\boldsymbol{f}'_{l+1}(=\boldsymbol{C}^T\boldsymbol{f}_{l+1})$ are the stiffness matrix and the external force vector after the degeneracy. The transformation matrix is constructed employing the scaling/wavelet functions in terms of the essential BCs. And, the matrix construction is carried out over a cell-based. An effective matrix operation can be carried out saving the computation time. After solving Eq.(35), the displacement vector $\boldsymbol{U}_{l+1}$ is derived with the relation of Eq.(34). The tying relation and the MPC equations can be developed when the wavelet functions of different resolution level are locally superposed on the scaling functions. The enforcement of the essential BCs with the different resolution models is validated with numerical examples.

3.3. Validation

The test problem presented in Fig.3 is analyzed using the proposed technique. Because the B-spline scaling/wavelet functions are non-orthogonal, higher bandwidth appears when multilevel wavelet functions are used in the WGM. The condition number of the stiffness matrix is also investigated. For

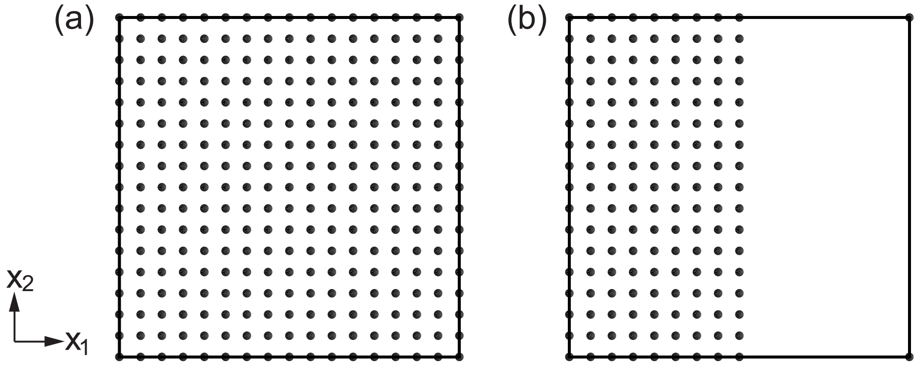

Figure 5: WG models for the rectangular plate (level-(l+3) model): (a) Uniform refinement (Model A) and (b) Partially refinement (Model B).

comparison, the test problem is again analyzed but using the penalty formulation in Eq.(15) for imposing the essential BCs instead.

Two different models are chosen. One is a uniformly refined model (Model A) and the other is a partially refined model (Model B). In Model A, all scaling and multilevel wavelet functions are employed while all scaling functions are adopted and the wavelet functions which located $x_1<1.0$ are used in Model B. The position of the nodes in Models A and B are presented in Figs.5 (a) and (b), respectively. The lowest resolution level is assumed as level-l and the spatial resolution of the level-l model is increased by adding the level-l, -$(l+1)$, $\cdots$ wavelet functions. They are the level-$(l+4)$ models. The displacements $u_1(\boldsymbol{x})$ and $u_2(\boldsymbol{x})$ at nodes 1, $\cdots$, 4 are examined to check the accuracy in the enforcements with the MPCs.

Table 1: Displacements of the level-$(l+4)$ model (Model A).

	MPCs(W)		pform3(W)	
Node no. $(x_1,\, x_2)$	$u_1(\boldsymbol{x})$	$u_2(\boldsymbol{x})$	$u_1(\boldsymbol{x})$	$u_2(\boldsymbol{x})$
Node 1 (0.0, 0.0)	0.0	0.0	0.0	0.1e-2
Node 2 (2.0, 0.0)	-0.6	0.0	-0.6	0.1e-2
Node 3 (0.0, 2.0)	0.0	2.0	0.0	-2.001
Node 4 (2.0, 2.0)	-0.6	2.0	-0.6	-2.001

The numerical results are presented in Tables 1 and 2 for Models A and

Table 2: Displacements of the level-$(l+4)$ model (Model B).

	MPCs(W)		pform3(W)	
Node no. (x_1, x_2)	$u_1(\boldsymbol{x})$	$u_2(\boldsymbol{x})$	$u_1(\boldsymbol{x})$	$u_2(\boldsymbol{x})$
Node 1 (0.0, 0.0)	0.0	0.0	0.0	0.1e-2
Node 2 (2.0, 0.0)	-0.6	0.0	-0.6	0.1e-2
Node 3 (0.0, 2.0)	0.0	2.0	0.0	-2.001
Node 4 (2.0, 2.0)	-0.6	2.0	-0.6	-2.001

B, respectively. MPCs(W) and pform3(W) are results with MPCs and the penalty formulation (α=1×10^3). In both cases, a uniform deformation is obtained. The coefficients of the level-l scaling functions have non-zero values, and all coefficients of the level-l to -$(l+3)$ wavelet functions become zero. Therefore, the analyses satisfy the MRA. The results of the penalty formulation have a small value which depend on α, although the essential BCs at the bottom and left sides of the plate close to zero to the limit of the machine precision. It is known that a numerical error invites in the WG analysis when the penalty parameter is too small. The error is converged as α becomes large. It is found that the essential BCs are exactly imposed when the MPCs are adopted, and the results with the penalty formulation approach to those with the MPCs when the parameter α increases.

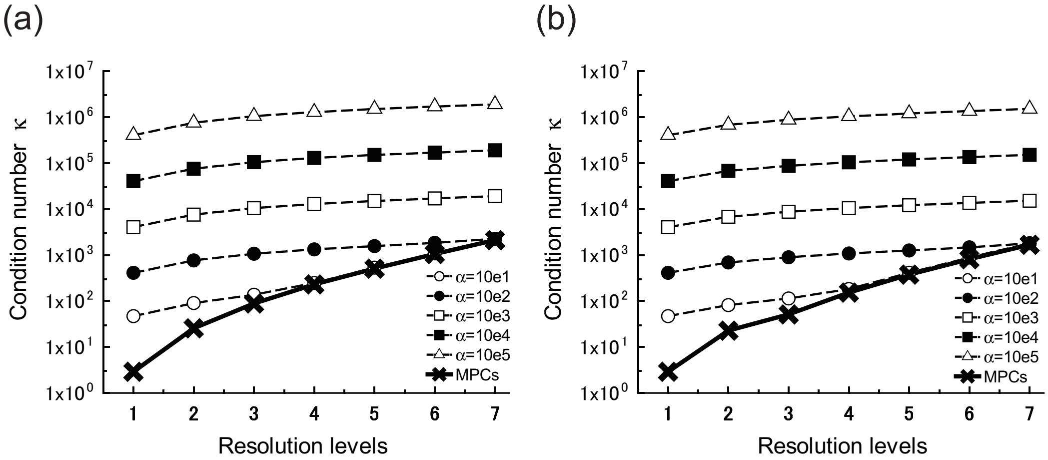

Figure 6: Condition numbers for different resolution models: (a) Uniform refinement (Model A) and (b) Partially refinement (Model B).

The condition number of the stiffness matrix is examined with the different resolution models. When analyzing the level-$(l+1)$ stiffness matrix $\boldsymbol{K}_{l+1}$, the condition number is defined as $\kappa(\boldsymbol{K}_{l+1})=|\lambda^{l+1}_{max}/\lambda^{l+1}_{min}|$. λ^{l+1}_{max} and λ^{l+1}_{min} are the maximum and minimum eigenvalues. For the penalty formulation, the level-$(l+1)$ stiffness matrix including a penalty term $(\boldsymbol{K}_{l+1}+\boldsymbol{K}^{\alpha}_{l+1})$ is analyzed. While the level-$(l+1)$ stiffness matrix of the MPC equations is analyzed, the degenerated stiffness matrix $\boldsymbol{K}'_{l+1}(=\boldsymbol{C}^T\boldsymbol{K}_{l+1}\boldsymbol{C})$ is solved. The spatial resolution of the level-l model is increased up to the level-$(l+6)$ model for Models A and B. The results are presented in Figs.6(a) and (b). The condition number from the penalty formulation is also presented, with the penalty parameter varied from α=1×10^1 to 1×10^5. The stiffness matrix become ill-conditioned as α gets large. Although the condition number gradually worsens as the spatial resolution increases in the MPCs enforcements, the value is less than the penalty formulation with α=1×10^3 even when the level-$(l+6)$ model is adopted.

In addition, the DOFs in the WG analyses are explored. The DOFs for Models A and B are presented in Tables 3 and 4. Because the stiffness matrix is degenerated based on the MPCs equations, there are fewer DOFs than in the WG analysis with the penalty formulation. Therefore, the MPCs is effective in enforcing the essential BCs as compared to the penalty formulation on this simple domain.

Table 3: DOFs for different resolution models : Model A.

Level	l	$l+1$	$l+2$	$l+3$	$l+4$	$l+5$	$l+6$
MPCs(W)	4	12	40	144	544	2,112	8,320
pform(W)	8	18	50	162	578	2,178	8,450

Table 4: DOFs for different resolution models : Model B.

Level	l	$l+1$	$l+2$	$l+3$	$l+4$	$l+5$	$l+6$
MPCs(W)	4	10	25	79	283	1,075	4,195
pform(W)	8	16	34	94	310	1,126	4,294

3.4. Treatment of external boundaries

In the WG discretization, a body is divided into equally spaced structural cells. The boundary of the analysis domain sometime cuts or partially cuts the cells. Here, the question of how to impose the essential BCs for such boundaries with MPCs is discussed.

An edge crack is modeled using the WGM. A half model is generated by employing symmetric boundary conditions. The crack length is given by a. The level-l and -$(l+1)$ models are schematically illustrated in Fig.7(a). The sizes of the level-l and -$(l+1)$ cells are also presented. The filled/open circles are nodes of the level-l scaling/wavelet functions, respectively. For the level-l model, a crack (a=L) can be modeled by imposing the essential BCs $u_2(\boldsymbol{x})$=0 on nodes A and B. For the level-$(l+1)$ model, an edge crack (a=$L/2$) is modeled by imposing the essential BCs on nodes C-F. In a similar manner, the displacements can be exactly fixed along the bottom edge when a crack tip locates on the nodes of the scaling/wavelet functions, as well as the square plate model discussed above. Although the essential BCs cannot exactly be imposed when the crack tip locates between the nodes. In such cases, the extended WGM [31-32] can be employed as an alternative way to treat a stationary crack and crack propagation simulations.

In the WGM, the equally spaced cells are divided into a number of sub-cells when the boundaries of the body partially cut the cells. The numerical integration of the stiffness matrix is carried out when the center of a sub-cell is located within the domain. For example, a rectangular domain is modeled by the sub-cell approach. The level-l and -$(l+1)$ models are shown in Fig.7(b). The WG models are 2D but the domain is cut by a simple geometry. Enforcement of the essential BCs along the bottom lines is examined using the 1D scaling/wavelet functions along the x_1-direction. The left hand boundary is located between nodes G and H in the level-l model, and nodes G-I are fixed to reproduce zero displacement at the bottom of the plate. In addition, the boundary is located at node H, node G is excluded from the stiffness matrix because the scaling function has zero value. For the level-$(l+1)$ model, the essential BCs on nodes J-N are needed to enforce zero displacement when the boundary is located between nodes J and K. Furthermore, when the boundary is located on node K, nodes K-N are fixed to impose the essential BCs. However, node K (level-l wavelet function) is excluded because a failure of linear independence would occur in the stiffness matrix [30]. In addition, if the boundary is located on node L, then node J is excluded. The WGMs with the scaling and multilevel wavelet functions pass the so-called patch test for the square plate problem. Therefore, the essential BCs can be imposed for a simple geometry by a combination of the scaling/wavelet functions appropriately.

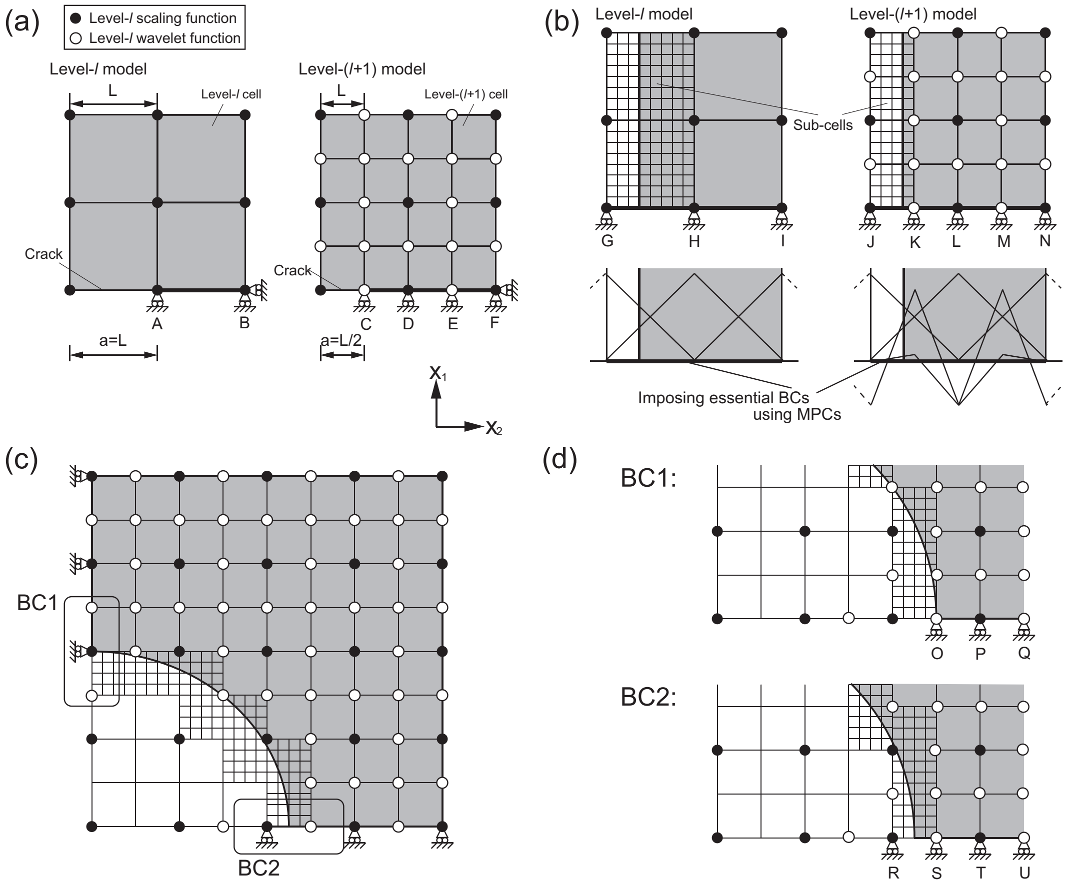

Figure 7: Treatment of external boundaries employing the MPCs in the WGM: (a) Edge crack problem, (b) Square plate problem, (c) Hole problem and (d) Close-up view of the hole edge and the enforcement of the essential BCs for BC1 and BC2.

The treatment of the essential BCs in the 2D case is discussed next. A square plate with a hole is presented in Fig.7(c). The level-$(l+1)$ model is used. The level-l wavelet functions are applied to the boundaries. The cells are cut or partially cut by the hole edge. Based on the discussion of the simple domain in Fig.7(b), the essential BCs are imposed along the left hand side and the bottom lines of the body. Two kinds of boundary are considered. The hole edge is located on the nodes of the scaling/wavelet functions (BC1), while the boundary is located between the nodes (BC2). In the case of BC1, nodes O-Q are fixed. And, the nodes R-U are fixed for BC2. When employing higher resolution wavelet functions, the essential BCs can be imposed in a similar way. The accuracy and effectiveness of the MPCs are examined with several numerical examples in the next section.

4. Numerical Examples

4.1. Multiresolution analysis

4.1.1. A center crack problem

To show the MPC enforcement, the MRA in the WGM is examined by considering a center crack of length $2a$ located in a square plate of 4.0×4.0 (mm). To model the cracked plate in the WGM, a quarter model 2.0×2.0 (mm) is chosen in situation with symmetrical boundary conditions. The Young's modulus is E=1.0 (MPa), and Poisson's ratio is ν=0.3. The plane stress condition is again assumed. The level-l model is presented in Fig.8(a). The analysis domain is divided into 2×2 level-l cells. To examine the MRA in the MPC enforcements, the level-$(l+3)$ model is adopted using the level-l scaling/wavelet functions, the level-$(l+1)$ and -$(l+2)$ wavelet functions. The nodes of the scaling/wavelet functions are presented in Fig.8(b). As the boundary conditions, $u_1(\boldsymbol{x})$ is fixed along the left hand side of the plate, and $u_2(\boldsymbol{x})$ is fixed along the bottom of the plate as shown in Fig.8(c). Four crack lengths a=0.5, 0.75, 0.875 and 1.0 (mm) are considered. The crack tips are located on the level-l, -$(l+1)$ and -$(l+2)$ wavelet functions, and the level-l scaling function, respectively. The WG models are called Models 1-4.

The stress distributions σ_{22} along the x_1-direction (MPCs(W)) are shown in Fig.9 for Models 1-4. To check the MRA, the WG analyses with the level-$(l+3)$ scaling functions (MPCs(S)) are also presented. They are good agreement with each other. The value of stress σ_{22} from the crack tip are presented in Tables 5-8 for Models 1-4, respectively. The same results are obtained with the same DOFs in the analyses of MPCs(W) and MPCs(S). Consequently, the MRA is confirmed in the crack problem. Furthermore, the results with the penalty formulations are presented. Two different penalty parameters α=1×10^3 (pform3(W)) and α=1×10^8 (pform8(W)) are chosen. DOFs of the WG analyses with the MPCs are less than those with the penalty formulation. The WG analyses with the penalty formulation approach those of the MPCs as the penalty parameter α increases.

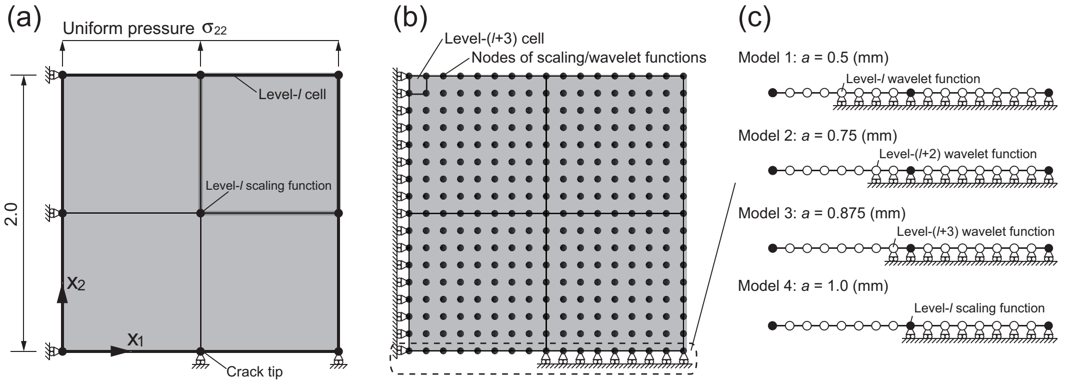

Figure 8: A center crack problem: (a) Level-l model, (b) Level-$(l+3)$ model (Uniform refinement) and (c) Essential boundary conditions for half crack lengths a=0.5, 0.75, 0.875 and 1.0 (mm).

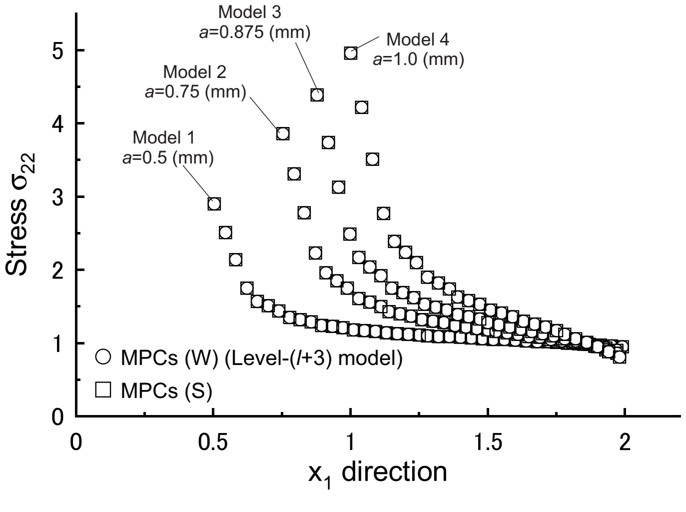

Figure 9: Stress distribution σ_{22} along x_1-direction for Models 1-4 (Level-$(l+3)$ model).

Table 5: Stress σ_{22} from the crack tip a=0.5 (mm) (Model 1).

	MPCs(W)	MPCs(S)	pform3(W)	pform8(W)
x_1\DOFs	548	548	578	578
0.5033	2.9012	2.9012	2.8750	2.9012
0.5123	2.8138	2.8138	2.7910	2.8138
0.5189	2.7499	2.7499	2.7296	2.7499
0.5279	2.6625	2.6625	2.6456	2.6625

Table 6: Stress σ_{22} from the crack tip a=0.75 (mm) (Model 2).

	MPCs(W)	MPCs(S)	pform3(W)	pform8(W)
x_1\DOFs	550	550	578	578
0.7533	3.8632	3.8632	3.8277	3.8632
0.7623	3.7386	3.7386	3.7078	3.7386
0.7689	3.6474	3.6474	3.6199	3.6474
0.7779	3.5228	3.5228	3.5000	3.5228

Table 7: Stress σ_{22} from the crack tip a=0.875 (mm) (Model 3).

	MPCs(W)	MPCs(S)	pform3(W)	pform8(W)
x_1\DOFs	551	551	578	578
0.8783	4.3903	4.3903	4.3499	4.3903
0.8873	4.2454	4.2454	4.2103	4.2454
0.8939	4.1392	4.1392	4.1081	4.1392
0.9029	3.9943	3.9943	3.9684	3.9943

Table 8: Stress σ_{22} from the crack tip a=1.0 (mm) (Model 4).

	MPCs(W)	MPCs(S)	pform3(W)	pform8(W)
x_1\DOFs	552	552	578	578
1.0033	4.9613	4.9613	4.9157	4.9613
1.0123	4.7942	4.7942	4.7546	4.7942
1.0189	4.6719	4.6719	4.6367	4.6719
1.0279	4.5048	4.5048	4.4756	4.5048

4.1.2. A square plate including a hole

A square plate with a hole is analyzed next. The accuracy of the WGM when the hole edge is located between the nodes of the scaling/wavelet functions is examined. The size of the plate is 4.0×4.0 (mm) and the radius of the hole is r_h. A quarter model with symmetrical boundary conditions is taken. The level-l model is presented in Fig.10(a). The plane stress condition is assumed, and the material properties are the same as in Section 4.1.1. The level-$(l+3)$ model is employed. For an example, nodal distribution of the analysis model with a hole r_h=1.0 (mm) is shown in Fig.10(b). To accurately represent the hole geometry, the level-l cell is divided into 128×128 sub-cells. Four different radii r_h=0.5, 0.67, 0.83 and 1.0 (mm) are employed to examine the MPCs enforcement. These are Models 1-4, respectively. The boundary conditions are presented in Fig.10(c). The hole edge in Models 1 and 4 are located on the level-l wavelet and scaling functions. In addition, the hole edge is located between nodes of the scaling/wavelet functions in Models 2 and 3, respectively. The essential BCs are imposed on the nodes based on the idea in Section 3.4.

The stress distributions σ_{22} are shown in Fig.11. The stresses are evaluated along the x_1-direction at the bottom of the plate. The MPCs(W) and MPCs(S) results are good agreement with each other. To further examine the numerical results, the values of the σ_{22} are presented in Tables 9-12. For Models 1 and 4, the stress values and DOFs of MPCs(W) are exactly same as for MPCs(S) and pform8(W). Therefore, the results have the MRA as well as the crack problem when the hole edge is located on the nodes of the scaling/wavelet functions. On the other hand, in Models 2 and 3, the DOFs and the results of MPCs(W) are slightly different from those of MPCs(S) and pform8(W). The results thus do not exactly satisfy the MRA. When employing MPCs in the WGM, the enforcement of the essential BCs is based on nodes of the scaling/wavelet functions, but the stiffness matrix is generated based on the cell and sub-cells. This is the reason why the WGM does not satisfy the MRA. When employing the penalty formulation, the essential BCs are accurately imposed and satisfy the MRA because the enforcement of the essential BCs is based on cell and sub-cells. The maximum stresses σ_{22} with the different resolution models is presented in Tables 13 and 14. The differences between MPCs(W) and pform8(W) become small as the spatial resolution increases because nodes of the scaling/wavelet functions increase along the boundaries.

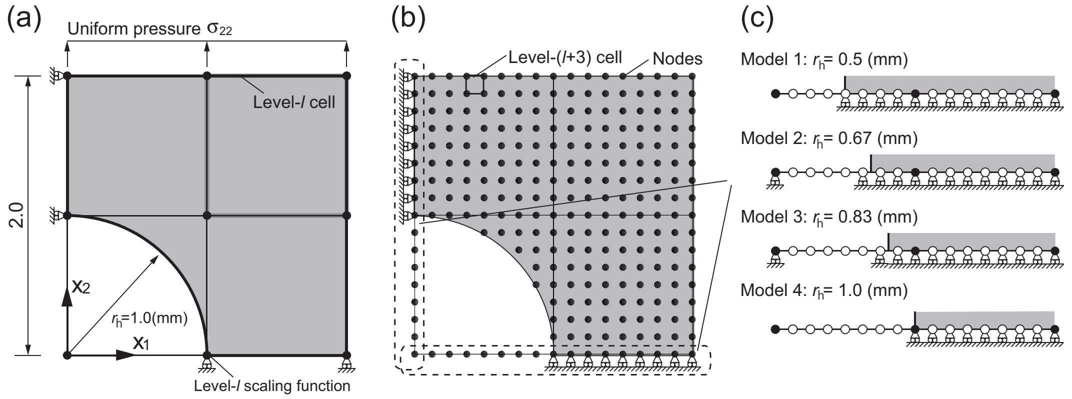

Figure 10: A hole problem: (a) Level-l model, (b) Level-(l+3) model (Uniform refinement) and (c) Essential boundary conditions for radii r_h=0.5, 0.67, 0.83 and 1.0 (mm).

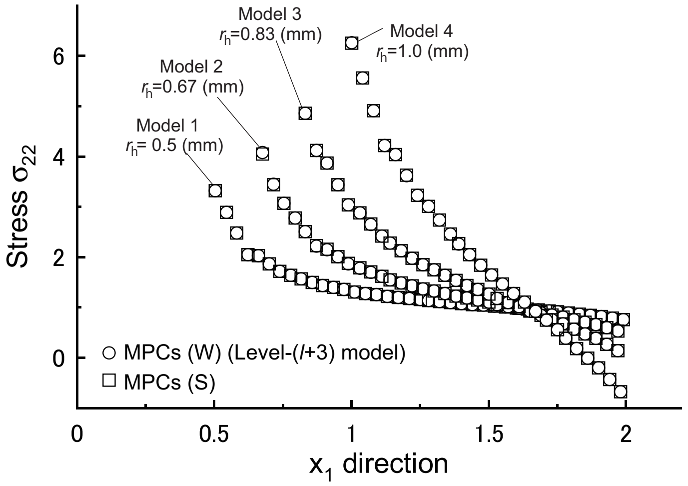

Figure 11: Stress distribution σ_{22} along x_1-direction for Models 1-4 (Level-($l+3$) model).

4.2. Adaptive analysis

One of the advantages of the WGM is its adaptive feature. The refinement of the solution can be performed effectively by superposing the high-resolution level wavelet functions. The accuracy of the MPC enforcements is

Table 9: Stress σ_{22} from the hole edge r_h=0.5 (mm) (Model 1).

	MPCs(W)	MPCs(S)	pform3(W)	pform8(W)
x_1\DOFs	536	536	562	562
0.5033	3.3233	3.3233	3.3174	3.3233
0.5123	3.2263	3.2263	3.2209	3.2263
0.5189	3.1552	3.1552	3.1502	3.1552
0.5279	3.0582	3.0582	3.0537	3.0582

Table 10: Stress σ_{22} from the hole edge r_h=0.67 (mm) (Model 2).

	MPCs(W)	MPCs(S)	pform3(W)	pform8(W)
x_1\DOFs	512	516	540	540
0.6752	4.0795	4.0538	4.0459	4.0538
0.6842	3.9394	3.9172	3.9104	3.9172
0.6908	3.8369	3.8172	3.8112	3.8172
0.6998	3.6968	3.6806	3.6757	3.6806

Table 11: Stress σ_{22} from the hole edge r_h=0.83 (mm) (Model 3).

	MPCs(W)	MPCs(S)	pform3(W)	pform8(W)
x_1\DOFs	496	500	522	522
0.8314	4.8620	4.8613	4.8582	4.8613
0.8404	4.6960	4.6954	4.6922	4.6954
0.8471	4.5745	4.5740	4.5707	4.5740
0.8561	4.4085	4.4081	4.4047	4.4081

Table 12: Stress σ_{22} from the hole edge r_h=1.0 (mm) (Model 4).

	MPCs(W)	MPCs(S)	pform3(W)	pform8(W)
x_1\DOFs	478	478	496	496
1.0033	6.2572	6.2572	6.2515	6.2572
1.0123	6.1016	6.1016	6.0965	6.1016
1.0189	5.9877	5.9877	5.9830	5.9877
1.0279	5.8321	5.8321	5.8279	5.8321

Table 13: Maximum stress σ_{22} for different resolution model r_h=0.67 (mm) (Model 2).

Level	l	$l+1$	$l+2$	$l+3$	$l+4$	$l+5$
MPCs(W)	1.3458	2.6364	3.5998	4.0795	4.1800	4.3509
pform8(W)	1.3458	2.6490	3.5926	4.0538	4.1814	4.3486

Table 14: Maximum stress σ_{22} for different resolution model r_h=0.83 (mm) (Model 3).

Level	l	$l+1$	$l+2$	$l+3$	$l+4$	$l+5$
MPCs(W)	1.5344	3.5274	4.6013	4.8620	4.8078	4.5499
pform8(W)	1.5344	3.4348	4.5510	4.8613	4.8056	4.5502

explored in the adaptive procedures dealing with several numerical examples for 2D elastic solids. The adaptive strategy proposed in [30] is taken. In the refinement procedures, the energy norm error is estimated over each cell, and one-step higher-resolution wavelet functions are superposed when the error is greater than a threshold. A criterion $\bar{\eta}_{cell}$=2.0% is defined. In addition, the error in strain energy W is evaluated in the adaptive analyses, and is defined, as: Error η=$|W$-$W^{Ref}|/W^{Ref}\times$100 (%). The reference solution W^{Ref} is derived from a commercial FEM solver with very fine mesh. MSC.Marc is employed, and the plane stress condition is assumed. Young's modulus and Poisson's ratio are E=30 (MPa) and ν=0.3 in all the examples.

4.2.1. A perforated infinite plate

A perforated infinite plate under remote stress σ_{11} is analyzed. The accuracy of the solution and condition number are examined when the different resolution level wavelet functions are placed locally. The model and the boundary conditions are sketched in Fig.12(a). The size of the square plate is 10×10 (mm) and the radius of the hole r_h=1.0 (mm). To consider an infinite domain under remote stress σ_{11}, traction boundaries are imposed along the top and right side of the plate. The stress components are given by

$$\begin{aligned}
\sigma_{11} &= 1 - \frac{1}{r^2}\left(\frac{3}{2}\cos 2\theta + \cos 4\theta\right) + \frac{3}{2r^4}\cos 4\theta, \\
\sigma_{22} &= -\frac{1}{r^2}\left(\frac{1}{2}\cos 2\theta - \cos 4\theta\right) - \frac{3}{2r^4}\cos 4\theta, \\
\sigma_{12} &= -\frac{1}{r^2}\left(\frac{1}{2}\sin 2\theta + \sin 4\theta\right) + \frac{3}{2r^4}\sin 4\theta, \qquad (36)
\end{aligned}$$

where (r,θ) are polar coordinates from the center of the hole. The square region is divided into 6×6 equally spaced structured cells, and the initial WG model is assumed as the level-l model. The WG adaptive analyses are carried out using MPCs(W), pform3(W) and pform8(W), respectively. To accurately represent the hole geometries, a level-l cell is divided into 128×128 sub-cells.

The spatial resolution of the WG model is increased up to level-($l + 5$). The nodal distribution of MPCs(W) is shown in Fig.12(b). All nodes on the bottom and left side of the plate are employed to accurately impose the essential BCs employing the MPCs. As the spatial resolution increases, the density of the nodes increases to represent the stress concentration around the hole. The stress distribution σ_{11} along the x_2-direction is shown. The solid line is the theoretical solution. As the refinement proceeds, the stress σ_{11} approaches the reference solution. A continuous stress distribution can be obtained in the adaptive WG models. The condition number is thus examined for MPCs(W), pform3(W) and pform8(W) with different resolution models. The results are presented in Table 15. As well as the uniform refinement models presented in Fig.6(a) and (b), the condition number from MPCs(W) is superior to the results from pform3(W) and pform8(W). In addition, the convergence of the adaptive analyses is examined in Fig.12(d) employing MPCs(W) and pform8(W). As a reference, the uniform refinement results are presented. Although the hole edge is located between nodes, and there are a few differences between MPCs(W) and pform8(W), the convergence rates are almost the same in the adaptive/uniform refinement models. As a consequence, it substantially confirms the effectiveness of the MPC enforcement in the WGM with adaptive analysis.

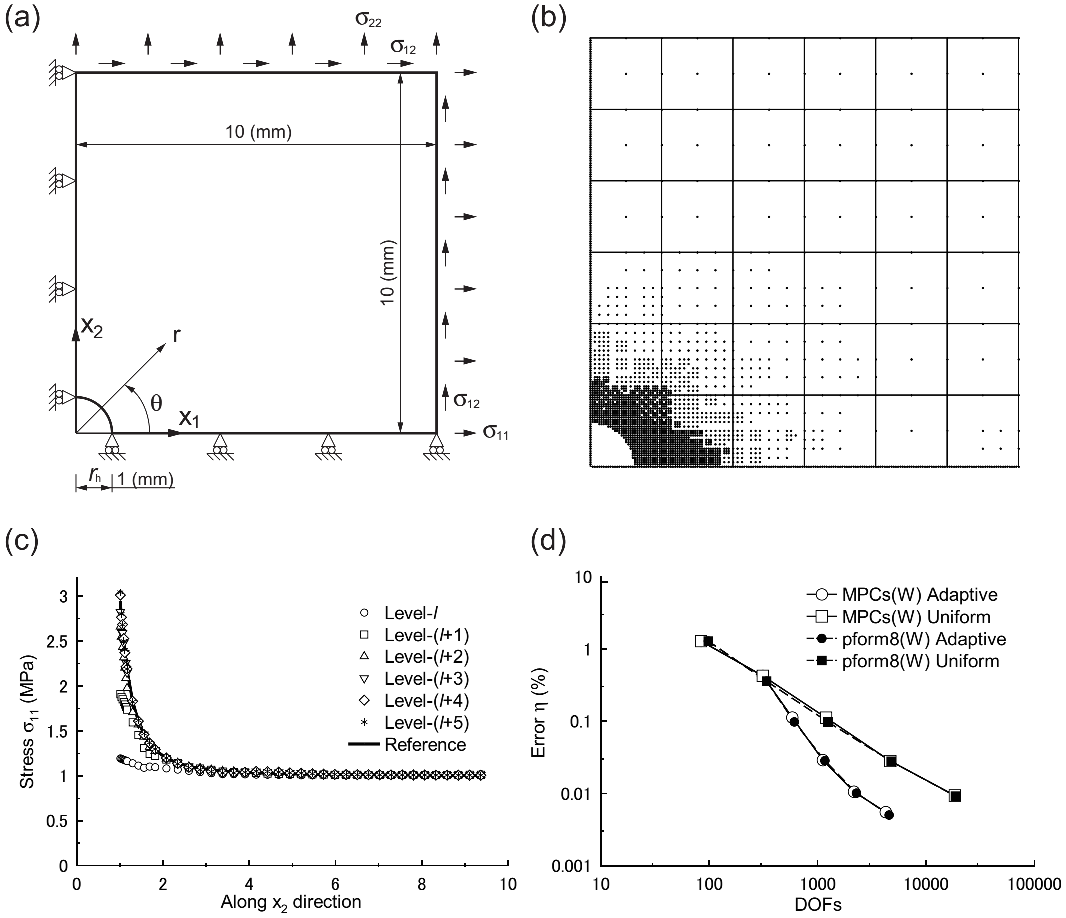

Figure 12: A perforated infinite plate under remote stress σ_{11}: (a) The model size and the boundary condition, (b) Level-($l+5$) adaptively refined model (MPCs(W)), (c) Stress distribution along x_2-direction (MPCs(W)) and (d) Convergence of the solution.

Table 15: Condition numbers of MPCs(W), pform3(W) and pform8(W).

Level	l	$l+1$	$l+2$	$l+3$	$l+4$	$l+5$
MPCs(W)	1.17E+02	4.97E+02	9.67E+02	4.14E+04	7.49E+04	1.54E+05
pform3(W)	1.59E+03	5.21E+04	6.75E+04	2.04E+06	2.76E+06	5.31E+06
pform8(W)	1.54E+08	5.00E+09	6.34E+09	1.87E+11	2.29E+11	2.55E+11

4.2.2. A cracked plate under pure mode-I

Next example deals with a cracked plate as schematically depicted in Fig.13(a). Severe stress concentration is generated near the crack tip in the numerical example. The size of the analysis domain is 2.0×1.0 (mm) and the crack length a=1.0 (mm). A symmetric boundary condition is employed. To impose pure mode-I deformation, traction boundaries are employed at the top, left and right side of the domain, as [50]:

$$\begin{aligned}
\sigma_{11} &= \frac{1}{\sqrt{r}}\cos\frac{\theta}{2}\left(1-\sin\frac{\theta}{2}\sin\frac{3\theta}{2}\right), \\
\sigma_{12} &= \frac{1}{\sqrt{r}}\cos\frac{\theta}{2}\left(1+\sin\frac{\theta}{2}\sin\frac{3\theta}{2}\right), \\
\sigma_{22} &= \frac{1}{\sqrt{r}}\sin\frac{\theta}{2}\sin\frac{\theta}{2}\sin\frac{3\theta}{2}, \qquad (37)
\end{aligned}$$

where (r,θ) is a polar coordinate from the crack tip. In the adaptive analysis, the analysis domain is divided into 20×10 equally spaced structured cells. The spatial resolution of the WG model (level-l model) is increased up to level-$(l+5)$. The WG analyses are carried out by MPCs(W) and pform8(W).

The distribution of the nodes is presented in Fig.13(b). As the refinement proceeds, the nodes of the wavelet functions are finer near the crack tip. The stress distribution σ_{22} along the x_1-direction for different resolution model is presented in Fig.13(c). As the reference solution, the theoretical value σ_{22} in Eq.(37) is used. It is confirmed that severe stress concentrations can be captured when the higher-resolution models are employed. In addition, continuous stress distribution can be obtained in all the WG models. Convergence of the solution is thus examined. The results are compared MPCs(W) with pform8(W), and are presented in Fig.13(c). Because the crack tip is located on the node of the scaling function, the error in the strain energy derived from both MPCs(W) and pform8(W) is found almost similarly. The DOFs of the MPCs(W) is slightly smaller than that of the pform8(W).

4.2.3. A rectangular plate with multiple holes

To analyze the WGMs including a complicated boundary condition, a plate with multiple holes is considered as the last numerical example. More precisely, a rectangular plate of 20×20 (mm) with multiple holes under biaxial loads as shown in Fig.14(a) is taken. The external loads are σ_{11}=σ_{22}=1.0

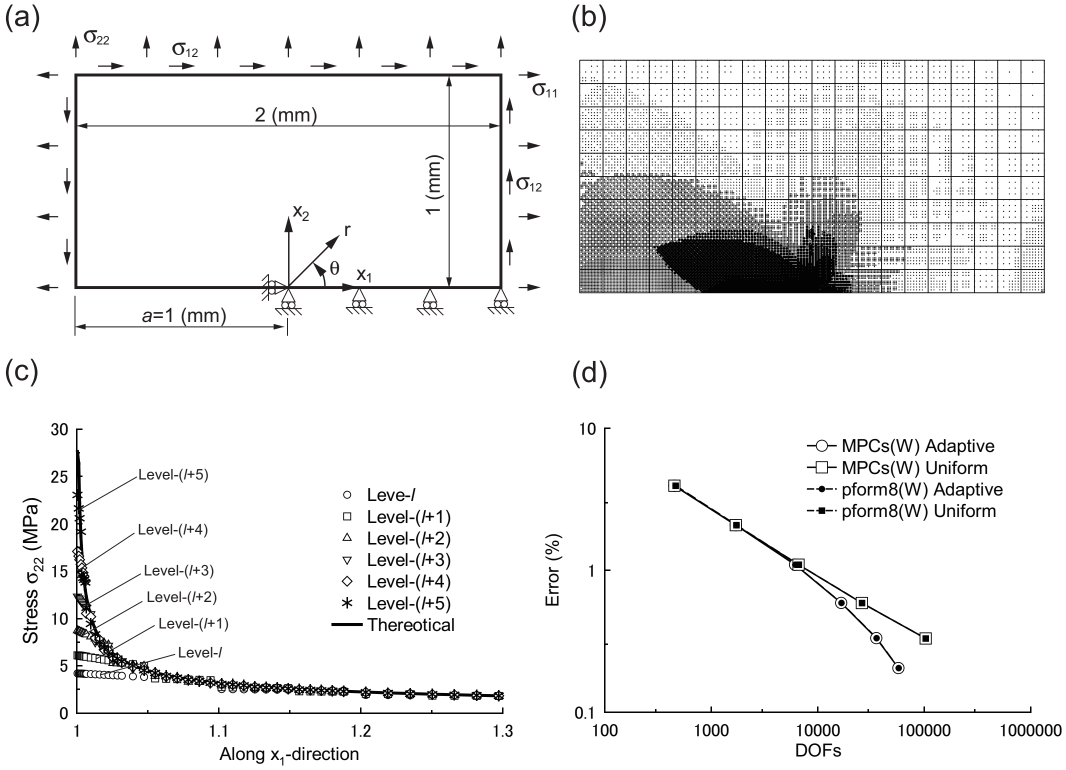

Figure 13: A cracked plate under pure mode-I: (a) The model size and the boundary condition, (b) Level-$(l+5)$ adaptively refined model (MPCs(W)), (c) Stress distribution along x_1-direction (MPCs(W)) and (d) Convergence of the solution.

(MPa). The size of the holes and the spacings are defined as shown in Fig.14(a). For symmetry of the problem, a quarter model is chosen. The analysis domain is divided into 10×10 equally spaced structured cells. The cell is the level-l cell. To accurately represent the hole geometries and the external boundaries, a level-l cell is divided into 256×256 sub-cells because the hole radii are small compare to the size of the level-l cell. The spatial resolution is increased up to level-$(l+5)$. The analyses are carried out using MPCs(W) and pform8(W). The accuracy and convergence of the solutions are numerically investigated.

The adaptively refined WG model (MPCs(W)) is presented in Fig.14(b). As the spatial resolution increases, the density of the nodes is refined near the holes. The stress distributions σ_{11} and σ_{22} along the x_1-direction of bottom of the quater model are presented in Fig.14(c). As the reference solution, FE results with a very fine mesh are employed. The stress distribution of the WGM is in good agreement with the results of the reference solution. The convergence of the solution are presented in Fig.14(d). The results from MPCs(W) match well with those from pform8(W) in the different resolution models.

Although a direct solver is employed for solving linear simultaneous equations of the WGM, convergence of the solution worsens when an ill-condition matrix is analyzed using an iterative solver. In the proposed technique, high accuracy computation can be carried out and the condition number of the stiffness matrix is improved compare to that of the penalty formulation. It is then found that the MPC enforcements is superior to the conventional technique in imposing the essential BCs of the spline-based WGM.

5. Conclusion

In this paper, MPCs are newly introduced to the spline-based WGM, considering adaptive analysis. The mathematical formulation and the numerical implementation were presented. The results were examined employing several numerical examples. When employing the MPC enforcements, the condition number of the stiffness matrix was improved as compared with the penalty formulation, and no additional DOFs were needed in the system of the simultaneous linear equations. The accuracy and effectiveness of the present formulation were demonstrated through a number of representative

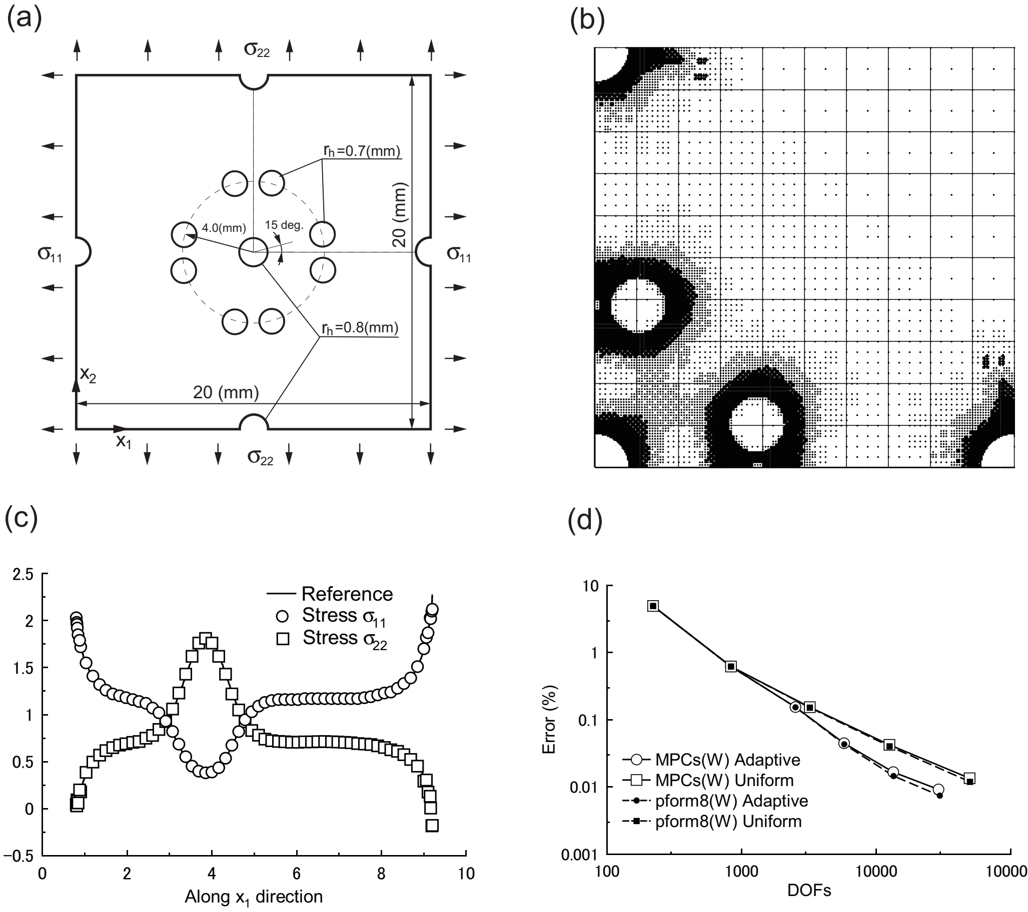

Figure 14: A rectangular plate with multiple holes: (a) Analysis model to be solved, (b) Level-$(l+5)$ adaptively refined model (MPCs(W)), (c) Stress distributions σ_{11} and σ_{22} along x_1-direction (MPCs(W)) and (d) Convergence of the solution.

numerical examples, showing a very good agreement. Different models of spatial resolution were numerically investigated, it was found that good results are gained by superposing finer wavelet functions locally. Furthermore, the convergence in error of strain energy was analyzed and it reveals a good performance of the proposed approach.

Acknowledgements

I would like to express my gratitude to Shuya Ueda (Graduate School of Engineering, Hiroshima University) for giving us valuable comments on this research. This research was supported in part by JSPS KAKENHI Grant-in-Aid for Scientific Research (B)(15H04212) and (C)(15K06632). Tinh Quoc Bui gratefully acknowledges support from Grant-in-Aid for Scientific Research-JSPS.

References

[1] C.K. Chui, An introduction to wavelets, Academic Press, San Diego, 1992.

[2] I. Daubechies, Ten lectures on wavelets, SIAM, Philadelphia, 1992.

[3] Y. Meyer, Wavelets: Algorithms and applications, SIAM, Philadelphia, 1993.

[4] C.K. Chui, Wavelets: A mathematical tool for signal analysis, SIAM, Philadelphia, 1997.

[5] S. Bertoluzza, G. Naldi, A wavelet collocation method for the numerical solution of partial differential equations, Appl. Comput. Harm. Anal. 3(1996)1-9.

[6] O.V. Vasilyev, S. Paolucci, A dynamically adaptive multilevel wavelet collocation method for solving partial differential equations in a finite domain, J. Comput. Phys. 125(1996)498-512.

[7] Y.-H. Zhou, J. Zhou, A modified wavelet approximation for multi-resolution AWCM in simulating nonlinear vibration of MDOF systems, Comput. Meth. Appl. Mech. Eng. 197(2008)1466-1478.

[8] Y.-H. Zhou, J. Zhou, A modified wavelet approximation of deflections for solving PDEs of beams and square thin plates, Finite. Elem. Anal. Des. 44(2008)773-783.

[9] I. Aziz, S.U. Islam, B. Šarler, Wavelets collocation methods for the numerical solution of elliptic BV problems, Appl. Math. Model. 37(2013)676-694.

[10] K. Koro, K. Abe, Non-orthogonal spline wavelets for boundary element analysis, Eng. Anal. Bound. Elem. 25(2001)149-164.

[11] K. Koro, K. Abe, A practical determination strategy of optimal threshold parameter for matrix compression in wavelet BEM, Int. J. Numer. Meth. Eng. 57(2003)169-191.

[12] K. Koro, K. Abe, A wavelet method for reducing the computational cost of BE-based homogenization analysis, Eng. Anal. Bound. Elem. 27(2003)439-454.

[13] W.-H. Chen, C.-W. Wu, A spline wavelets element method for frame structures vibration, Comput. Mech. 16(1995)11-21.

[14] J. Ko, A.J. Kurdila, M.S. Pilant, A class of finite element methods based on orthonormal, compactly supported wavelets, Comput. Mech. 16(1995)235-244.

[15] J.W. Xiang, X.F. Chen, Z.J. He, H.B. Dong, The construction of 1D wavelet finite elements for structural analysis, Comput. Mech. 40(2007)325-339.

[16] X. Chen, J. Xiang, B. Li, Z. He, A study of multiscale wavelet-based elements for adaptive finite element analysis, Adv. Eng. Software. 41(2010)196-205.

[17] Z. Yang, X. Chen, X. Zhang, Z. He, Free vibration and buckling analysis of plates using B-spline wavelet on the interval Mindlin element, Appl. Math. Model. 37(2013)3449-3466.

[18] H. Zuo, Z. Yang, X. Chen, Y. Xie, H. Miao, Analysis of laminated composite plates using wavelet finite element method and higher-order plate theory, Compos. Struct. 131(2015)248-258.

[19] X. Zhang, H. Zuo, J. Liu, X. Chen, Z. Yang, Analysis of shallow hyperbolic shell by different kinds of wavelet elements based on B-spline wavelet on the interval, Appl. Math. Model. 40(2016)1914-1928.

[20] Z.-B. Yang, X.-F. Chen, Y. Xie, H. Zuo, H.-H. Miao, X.-W. Zhang, Wave motion analysis and modeling of membrane structures using the wavelet finite element method, Appl. Math. Model. 40(2016)2407-2420.

[21] K. Amaratunga, J.R. Williams, S. Qian, J. Weiss, Wavelet-Galerkin solutions for one-dimensional partial differential equations, Int. J. Numer. Meth. Eng. 37(1994)2703-2716.

[22] S. Bertoluzza, Y. Maday, J.C. Ravel, A dynamically adaptive wavelet method for solving partial differential equations, Comput. Meth. Appl. Mech. Eng. 116(1994)293-299.

[23] Z. Youhe, W. Jizeng, Z. Xiaojing, Applications of wavelet Galerkin FEM to bending of beam and plate structures, Appl. Math. Mech. 19(1998)745-755.

[24] Y. Liu, L. Sun, Y. Liu, Z. Cen, Multi-scale B-spline method for 2-D elastic problems, Appl. Math. Model. 35(2011)3685-3697.

[25] B. Li, X. Chen, Wavelet-based numerical analysis: A review and classification, Finite. Elem. Anal. Des. 81(2014)14-31.

[26] G.C.A. DeRose Jr., A.R. Díaz, Solving three-dimensional layout optimization problems using fixed scale wavelets, Comput. Mech. 25(2000)274-285.

[27] P. Venini, P. Morana, An adaptive wavelet-Galerkin method for an elastic-plastic-damage constitutive model: 1D problem, Comput. Meth. Appl. Mech. Eng. 190(2001)5619-5638.

[28] L. Zhang, J. Wang, Y.-H. Zhou, Wavelet solution for large deflection bending problems of thin rectangular plates, Arch. Appl. Mech. 85(2015)355-365.

[29] M.R. Yousefi, R. Jafari, H.A. Moghaddam, Imposing boundary and interface conditions in multi-resolution wavelet Galerkin method for numerical solution of Helmholtz problems, Comput. Meth. Appl. Mech. Eng. 276(2014)67-94.

[30] S. Tanaka, H Okada, S. Okazawa, A wavelet Galerkin method employing B-spline bases for solid mechanics problems without the use of a fictitious domain, Comput. Mech. 50(2012)35-48.

[31] S. Tanaka, H. Okada, S. Okazawa, M. Fujikubo, Fracture mechanics analysis using the wavelet Galerkin method and extended finite element method, Int. J. Numer. Meth. Eng. 93(2013)1082-1108.

[32] S. Tanaka, T. Kawahara, H. Okada, Study on crack propagation simulation of surface crack in welded joint structure, Mar. Struct. 39(2014)315-334.

[33] S. Tanaka, H. Suzuki, S. Ueda, S. Sannomaru, An extended wavelet Galerkin method with a high-order B-spline for 2D crack problems, Acta. Mech. 226(2015)2159-2175.

[34] S. Tanaka, S. Sannomaru, M. Imachi, S. Hagihara, S. Okazawa, H. Okada, Analysis of dynamic stress concentration problems employing spline-based wavelet Galerkin method, Eng. Anal. Bound. Elem. 58(2015)129-139.

[35] A.R. Diaz, A wavelet-Galerkin scheme for analysis of large-scale problems on simple domains, Int. J. Numer. Meth. Eng. 44(1999)1599-1616.

[36] X. Chen, S. Yang, J. Ma, Z. He, The construction of wavelet finite element and its application, Finite. Elem. Anal. Des. 40(2004)541-554.

[37] J.-G. Han, W.-X. Ren, Y. Huang, A spline wavelet finite-element method in structural mechanics, Int. J. Numer. Meth. Eng. 66(2006)166-190.

[38] T. Belytschko, Y.Y. Lu, L. Gu, Element-free Galerkin methods, Int. J. Numer. Meth. Eng. 37(1994)229-256.

[39] H. Noguchi, T. Kawashima, T. Miyamura, Element free analyses of shell and spatial structures, Int. J. Numer. Meth. Eng. 47(2000)1215-1240.

[40] S. Tanaka, H. Suzuki, S. Sadamoto, M. Imachi, T.Q. Bui, Analysis of cracked shear deformable plates by an effective meshfree plate formulation, Eng. Fract. Mech. 144(2015)142-157.

[41] S. Tanaka, H. Suzuki, S. Sadamoto, S. Sannomaru, T.T. Yu, T.Q. Bui, J-integral evaluation for 2D mixed-mode crack problems employing a meshfree stabilized conforming nodal integration method, Comput. Mech. 58(2016)185-198.

[42] Y.Y. Lu, T. Belytschko, L. Gu, A new implementation of the element free Galerkin method, Comput. Meth. Appl. Mech. Eng. 113(1994)397-414.

[43] T. Nagashima, Node-by-node meshless approach and its applications to structural analyses, Int. J. Numer. Meth. Eng. 46(1999)341-385.

[44] T. Nagashima, Development of a CAE system based on the node-by-node meshless method, Comput. Meth. Appl. Mech. Eng. 187(2000)1-34.

[45] S. Sadamoto, S. Tanaka, S. Okazawa, Elastic large deflection analysis of plates subjected to uniaxial thrust using meshfree Mindlin-Reissner formulation, Comput. Mech. 52(2013)1313-1330.

[46] J.S. Chen, H.P. Wang, New boundary condition treatments in meshfree computation of contact problems, Comput. Meth. Appl. Mech. Eng. 187(2000)441-468.

[47] J.G. Wang, G.R. Liu, A point interpolation meshless method based on radial basis functions, Int. J. Numer. Meth. Eng. 54(2002)1623-1648.

[48] T.Q. Bui, T.N. Nguyen, H. Nguyen-Dang, A moving Kriging interpolation-based meshless method for numerical simulation of Kirchhoff plate problems, Int. J. Numer. Meth. Eng. 77(2009)1371-1395.

[49] N.T. Nguyen, T.Q. Bui, C. Zhang, T.T. Truong, Crack growth modeling in elastic solids by the extended meshfree Galerkin radial point interpolation method, Eng. Anal. Bound. Elem. 44(2014)87-97.

[50] S.N. Atluri, Computational Methods in the Mechanics of Fracture, Elsevier North-Holland: Amsterdam, 1986.